Title
Electrostatic-Attraction-Driven Self-Assembled Graphene-Disordered Rocksalt Composite Cathode for Lithium-Ion Batteries

Journal
Advanced Functional Materials

ISSN
1616-301X

Authors
Avvaru, Venkata Sai
Zuba, Mateusz
Armstrong, Beth L
et al.

Publication Date
2026-07-10

DOI
10.1002/adfm.76964

Peer reviewed

Advanced Functional Materials

ADVANCED FUNCTIONAL MATERIALS
www.afm-journal.de

RESEARCH ARTICLE OPEN ACCESS

Electrostatic-Attraction-Driven Self-Assembled Graphene-Disordered Rocksalt Composite Cathode for Lithium-Ion Batteries

Venkata Sai Avvaru[1] | Mateusz Zuba[2] | Beth L. Armstrong[3] | Shilong Wang[1,4] | Minh X. Tran[5] | Bernardine L. D. Rinkel[5,6] | Finn Babbe[7] | Harshita Lohani[1] | Yanbao Fu[5] | Isik Su Buyuker[2] | Vincent Battaglia[5] | Ozgenur Kahvecioglu[2] | Robert Kostecki[5] | Bryan D. McCloskey[5,6] | Haegyeom Kim[1]

[1]Materials Sciences Division, Lawrence Berkeley National Laboratory, Berkeley, California, USA | [2]Applied Materials Division, Argonne National Laboratory, Lemont, Illinois, USA | [3]Materials Science and Technology Division, Oak Ridge National Laboratory, Oak Ridge, Tennessee, USA | [4]Department of Materials Science and Engineering, UC Berkeley, Berkeley, California, USA | [5]Energy Technologies and Systems Division, Lawrence Berkeley National Laboratory, Berkeley, California, USA | [6]Department of Chemical and Biomolecular Engineering, University of California, Berkeley, California, USA | [7]Chemical Sciences Division, Lawrence Berkeley National Laboratory, Berkeley, California, USA

Correspondence: Haegyeom Kim (haegyumkim@lbl.gov)

Received: 8 January 2026 | **Revised:** 11 June 2026 | **Accepted:** 23 June 2026

Keywords: carbon composite | cathodes | disordered rocksalt | graphene | lithium-ion batteries | solution-based synthesis

ABSTRACT

Disordered rocksalt cathodes hold promise for achieving high-capacity lithium-ion batteries while using low-cost, earth-abundant elements. However, their electrochemical performance remains critically limited by their poor electronic conductivity. Conventional strategies such as high-energy ball milling with excess carbon additives can improve conductivity but remain challenging to scale and often produce defects and increase surface area, thereby accelerating capacity degradation. Herein, we report an alternative approach of electrostatic-attraction-driven self-assembly to fabricate $Li_{1.2}Mn_{0.6}Ti_{0.2}O_{1.8}F_{0.2}$ (LMTOF) particles uniformly wrapped with electronically conductive graphene sheets without associated materials degradation. The graphene-wrapped LMTOF demonstrates significantly improved cycling stability (89% capacity retention after 100 cycles) and superior rate capability compared with an LMTOF-carbon composite electrode fabricated using the conventional high-energy ball-milling process. Post-cycling analysis reveals reduced oxygen evolution, suppressed unwanted side reactions, and improved structural integrity for the graphene-LMTOF composite. This work highlights the advantages of solution-based carbon wrapping and offers a scalable strategy to prepare high-performance DRX cathodes for lithium-ion batteries.

1 | Introduction

Disordered rock salt (DRX) cathode materials have emerged as promising candidates for next-generation lithium-ion batteries (LIBs) owing to their structural flexibility and high-energy density [1–5]. Unlike conventional layered oxide cathodes, which consist of ordered and separated Li and transition metal (TM) slabs, DRX materials adopt a cation-disordered cubic structure that enables the incorporation of a wide range of TMs [1, 6, 7]. This structural flexibility promotes the use of earth-abundant and cost-effective elements such as manganese (Mn) and iron (Fe), reducing the dependence on critical metals such as nickel (Ni) and cobalt (Co), which are essential components of traditional layered oxide systems [1, 6–11]. In this respect, the DRX class of materials provides a pathway for more environmentally benign and cost-effective cathode development. Among various

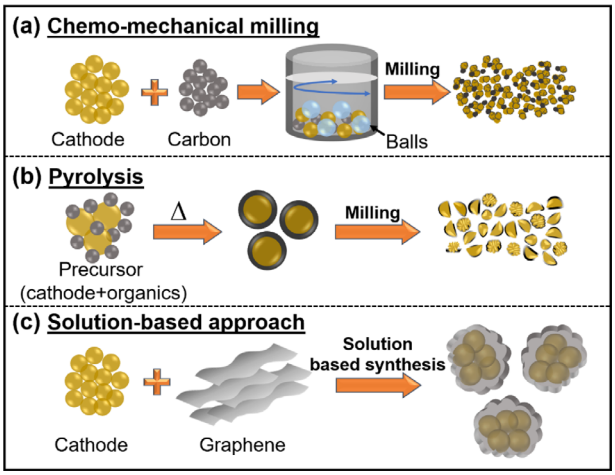

FIGURE 1 | Schematic representation of (a) high-energy ball milling process for carbon-cathode composite fabrication, (b) conventional pyrolysis carbon coating, and (c) solution-based electrostatic self-assembly method for graphene wrapping.

DRX materials, Mn-based compositions have shown particularly promising electrochemical performance, offering high capacities and energy densities [1–3, 9, 12–14]. Recent theoretical studies have also shown that the DRX framework is applicable beyond Li systems, with similar cation-distribution principles extending to Na-ion DRX cathodes as well [15].

However, the widespread adoption of DRX cathodes has been hindered by their intrinsically low electronic and ionic conductivities [7, 16, 17]. To mitigate these limitations, substantial amounts of conductive carbon additives and intensive high-energy ball milling are typically required during electrode fabrication. The objective of these processes is to reduce the particle size and ensure uniform carbon distribution, which are essential for achieving acceptable rate performance and capacity retention (Figure 1a) [2, 3, 9, 14, 17, 18]. Recently, various strategies have been proposed to enhance the electronic conductivity of DRX materials. For example, Xu et al. employed a vapor-phase technique to deposit an amorphous carbon coating on $Li_{1.2}Mn_{0.4}Ti_{0.4}O_2$ particles, improving their electronic conductivity [19]. Patil et al. systematically explored the influence of the carbon microstructure and ratio on the electrochemical behaviors of $Li_{1.2}Mn_{0.5}Ti_{0.3}O_{1.9}F_{0.1}$, ultimately developing a graphitic carbon-coated cathode that exhibited enhanced cycling stability [20]. Zhou et al. synthesized carbon-coated $Li_{1.2}Mn_{0.2}Ti_{0.6}O_2$ via a pyrolysis process, utilizing sucrose as the carbon source (Figure 1b) [21]. Although these techniques have shown some progress in improving the performance of DRX materials, they still rely on intensive high-energy dry ball milling or shaker milling combined with a substantial amount of carbon additives during electrode preparation. The post-milling process can result in cracking of the coated carbon layer. In addition, while effective in boosting the electronic conductivity, dry milling-based approaches remain challenging to scale because of low yield, and they may introduce surface and bulk defects in the cathode particles due to the highly energy-intensive process. These defects can accelerate performance degradation during repeated lithium (de)intercalation cycles, ultimately limiting the long-term stability and practical viability of DRX cathodes.

Solution-based electrostatic self-assembly processes, where particles or molecules with opposite electrical charges spontaneously form complexes, have been broadly applied in nanoparticle superlattices, polymer complex, organic–inorganic hybrids, and carbon–inorganic composites [22–25]. Inspired by these composite developments, we explored aqueous-solution-based synthesis approaches for reduced graphene oxide (rGO) wrapping over DRX particles and achieved uniform distribution [7]. Such a solution-based process could offer a more controllable way to apply carbon wrapping (Figure 1c) [26–28]. However, an aqueous-solution process leads to metal-ion dissolution, Li^+/H^+ exchange, and corresponding structural degradation, ultimately compromising the electrochemical performance and cycling stability of the DRX cathode, which remains an important challenge.

In this work, we present a non-aqueous solution-based wrapping approach using tetrahydrofuran (THF) as the solvent to fabricate graphene-wrapped $Li_{1.2}Mn_{0.6}Ti_{0.2}O_{1.8}F_{0.2}$ (LMTOF) particles. THF was selected based on a systematic screening of non-aqueous solvents for their ability to disperse graphene, maintain chemical compatibility with LMTOF cathodes, and sustain favorable surface-charge interactions. This approach employs electrostatic attraction between positively charged polyethylenimine (PEI)-coated LMTOF particles and negatively charged graphene, resulting in graphene-wrapped LMTOF (GrPLMTOF). Our method does not require any high-energy mechanical processing during electrode preparation, thereby avoiding particle fracture, defect formation, and carbon-particle detachment. This strategy addresses a key challenge in DRX cathode development by providing a robust electronically conductive carbon network while fully preserving the structural integrity of the DRX particles. Importantly, our approach provides an alternative and potentially scalable carbon-wrapping method for DRX compounds, offering a practically viable solution that avoids the limitations of dry ball milling used in earlier DRX studies [3, 19, 20, 29, 30]. The GrPLMTOF composite exhibited enhanced cycling stability and rate capability compared with conventionally prepared ball-milled carbon-LMTOF composites. Post-cycling analysis demonstrated improved structural retention and minimized oxygen evolution in the graphene-wrapped composite.

2 | Results

2.1 | Solvent Screening for Graphene-Disordered Rock-Salt Oxide Composite Synthesis

To develop graphene-wrapped disordered rock-salt oxide composites, we first screened potential processing solvents. In our previous work, we demonstrated the success of an aqueous solution process in producing graphene wrapping over LMTOF particles [7]; however, metal-ion leaching and Li^+/H^+ exchange resulted in degradation of the LMTOF structure and its electrochemical performance. Therefore, we needed to identify an alternative processing solvent. The ideal non-aqueous solvent should (i) ensure effective graphene dispersion, (ii) have good chemical compatibility with LMTOF, and (iii) preserve the positively charged surfaces of PEI-coated LMTOF particles.

To identify a promising non-aqueous solvent for graphene wrapping, several candidates, including dimethylformamide (DMF),

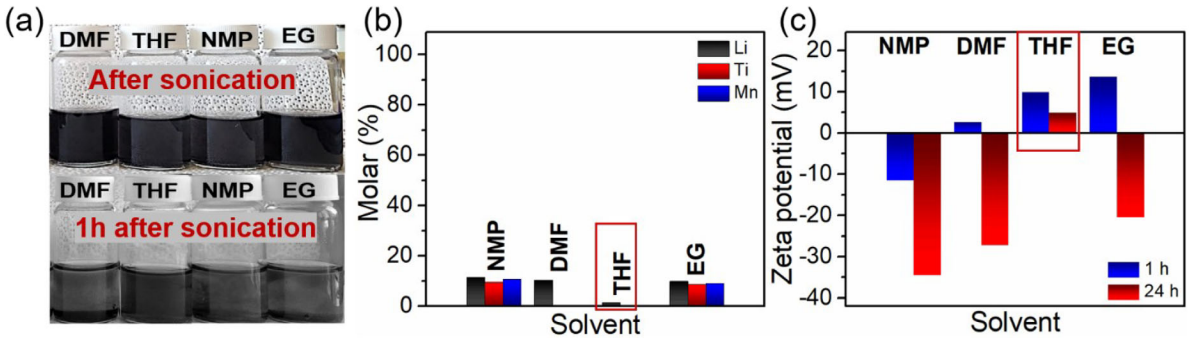

FIGURE 2 | (a) Photo images of graphene dispersion in DMF, THF, NMP, and EG after sonication and 1 h after sonication. (b) ICP-MS results of solvents after LMTOF dispersion. (c) Zeta potential analysis of PEI-coated LMTOF in various solvents.

tetrahydrofuran (THF), N-methylpyrrolidone (NMP), and ethylene glycol (EG), were evaluated, as shown in Figure 2. These solvents were initially selected because of their known ability to disperse carbon [31–35]. For the graphene-dispersion testing, graphene (5 mg) was dispersed in each solvent in equal amounts (0.5 mg/mL) and sonicated for 1 h. All the solvents showed good dispersion of graphene sheets immediately after sonication. However, agglomerated graphene sheets were observed in the DMF and EG solvents after resting for 1 h, whereas THF and NMP maintained a stable graphene dispersion even after resting for 1 h (Figure 2a). The chemical compatibility of LMTOF with these solvents was assessed using inductively coupled plasma mass spectrometry (ICP-MS) after 24 h of dispersion of LMTOF, as shown in Figure 2b. LMTOF exhibited much reduced metal-ion leaching in these solvents compared to that in water [7]; however, substantial metal-ion leaching was still observed in DMF, EG, and NMP, with Li dissolution of 10%, 9%, and 11%, respectively; Mn dissolution of 0.2%, 9%, and 10%, respectively; and Ti dissolution of 0.2%, 8%, and 9%, respectively. In sharp contrast, no detectable Mn and Ti dissolution and negligible Li dissolution were observed for THF, indicating its excellent chemical compatibility with LMTOF. Lastly, zeta potential measurements (Figure 2c) were performed to evaluate the surface charge of the PEI-coated LMTOF in these solvents. The PEI-coated LMTOF revealed a positive surface charge in THF, DMF, and EG after 1 h of dispersion. However, the PEI-coated LMTOF exhibited a negative surface charge in NMP solvent after 1 h, which likely indicates that the PEI coating layer is readily dissolved in the NMP solvent. The surface charge of the PEI-coated LMTOF changed from positive (+) to negative (−) after 24 h in the DMF and EG solvents. In contrast, THF retained a positive charge of the PEI-coated LMTOF even after 24 h. It is likely that strong polar solvents (such as NMP, DMF, and EG) dissolve the PEI coating layer, whereas THF, a moderately polar solvent, neither dissolves nor washes away the PEI coating layer. As a result, we identified THF as the most suitable solvent for the non-aqueous synthesis process based on its graphene dispersion-ability, chemical compatibility with LMTOF, and surface-charge retention.

2.2 | Graphene-Wrapped Disordered Rock-Salt Oxide Composite Development

In this study, LMTOF powder was selected as a model system for the graphene composite and synthesized via a conventional solid-state method, following a previously reported procedure [36]. The graphene-wrapped LMTOF was fabricated using a solution-based wrapping process, in which a uniform graphene wrapping over PEI-coated LMTOF (GrPLMTOFP) was achieved by utilizing the positively charged PEI-coated LMTOF and negatively charged graphene in THF solvent. Herein, we used 10 wt.% graphene in the composite GrPLMTOFP development. Figure 3a–c presents scanning electron microscopy (SEM) images of LMTOF and GrPLMTOFP. The pristine LMTOF in Figure 3a exhibits a bimodal particle size distribution of 0.2–0.5 μm and 0.5–2 μm, along with aggregated secondary particles, which is consistent with the particle size analysis (Figure S1). In contrast, the GrPLMTOF in Figure 3b,c displays thin graphene sheets uniformly wrapped over the PEI-coated LMTOF particles. The energy-dispersive X-ray spectroscopy (EDS) mapping in Figure S2 further confirms the uniform carbon coverage over the LMTOF particles. The graphene content in the composite after the synthesis was verified to be ~10.2 wt.% using a carbon analyzer.

The GrPLMTOF composite was subjected to a moderate-temperature heat treatment (200°C to 400°C) in Ar atmosphere to remove residual surface functional groups on graphene. X-ray diffraction (XRD) patterns of the GrPLMTOFP composites that were heat-treated at 200°C (denoted as GrPLMTOF200), 300°C (denoted as GrPLMTOF300), and 400°C (denoted as GrPLMTOF400) are shown in Figure 3d along with those of the pristine LMTOF and GrPLMTOF (without heat treatment). The XRD patterns of GrPLMTOF, GrPLMTOF200, and GrPLMTOF300 retained the characteristic peaks of the DRX structure with no significant shift or secondary phases, indicating the preserved structural integrity. However, the GrPLMTOF400 composite displayed peak shifts at ~43° and ~63° toward higher two-theta angles and additional peaks at ~18° and ~36°. These results indicate that heat treatments up to 300°C preserve the DRX structure, whereas higher temperatures induce structural degradation. X-ray photoelectron spectroscopy (XPS) analysis of the C 1s region (Figure 3e) was performed to investigate the effect of heat treatment on reducing the surface functional groups of graphene. GrPLMTOF without heat treatment exhibited characteristic peaks at ~284.5 eV (C—C) and ~288.5 eV (O—C═O) [37, 38]. Upon thermal treatment, a substantial reduction of the oxygen-containing carbon species was observed. This result confirms the removal of oxygen-containing functionalities and the formation of a chemically stable, conductive graphene interface facilitated by the thermal treatment. Raman spectroscopy was

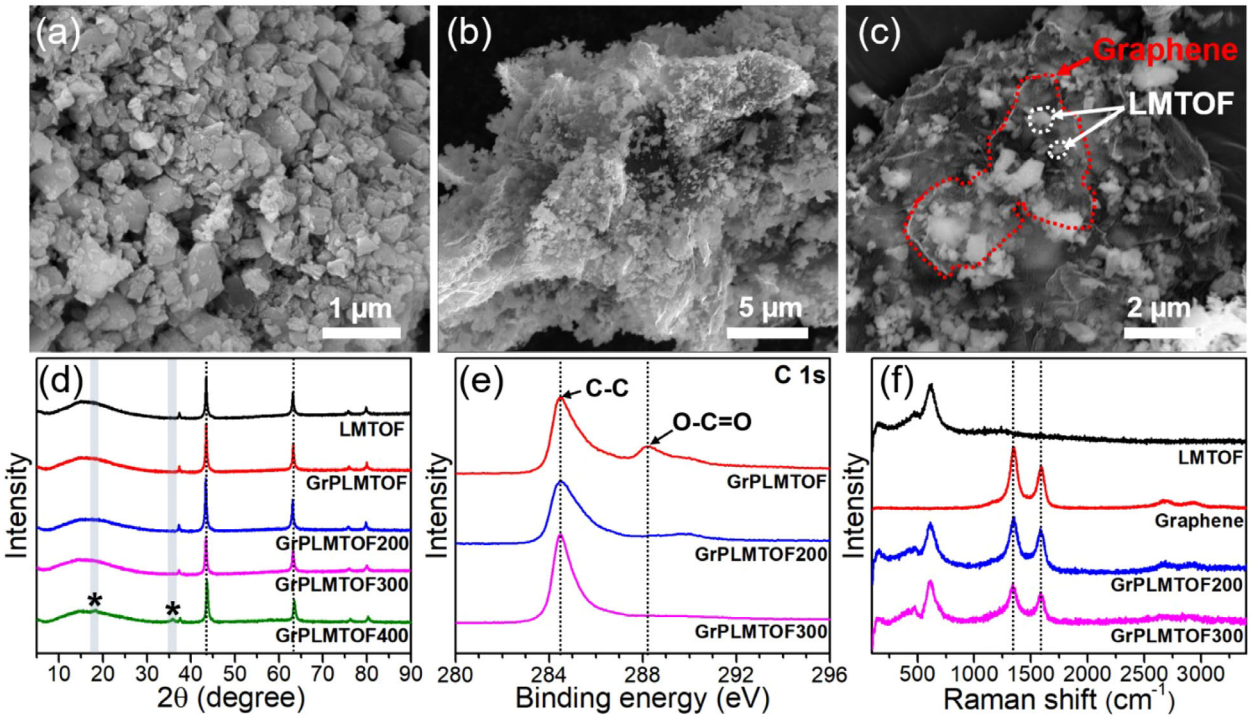

FIGURE 3 | SEM images of (a) pristine LMTOF and (b,c) GrPLMTOF. (d) XRD analysis and (e) C1s XPS of GrPLMTOF with varied heat treatment. (f) Raman spectra of pristine LMTOF, graphene, and GrPLMTOF200.

further used to investigate the structural characteristics of graphene in the GrPLMTOF200 composite. Figure 3f presents the Raman analysis results of LMTOF, graphene, and the GrPLMTOF200 composite. The GrPLMTOF200 exhibited characteristic D (~1350 cm^{-1}) and G (~1580 cm^{-1}) bands of graphene [39] and typical Raman spectra of DRX compounds [40, 41]. Interestingly, the intensity ratio of D and G bands (I_d/I_g) decreased from 1.25 in graphene to 1.178 and 1.180 in GrPLMTOF200 and GrPLMTOF300, respectively. This I_d/I_g decrease indicates a lower defect density, likely due to thermally induced structural rearrangement, where disordered carbon regions realign into a more ordered sp^2 configuration and residual functional groups are removed [39, 42, 43], which is in good agreement with the XPS results.

2.3 | Electrochemical Performance of Graphene-Wrapped PEI-Coated LMTOF Composites

We first evaluated the electrochemical performance of the graphene-wrapped PEI-coated LMTOF composites with varied heat-treatment temperatures, as shown in Figure S3. All the cells were tested in Li-metal half-cells at a current rate of 20 mA g^{-1} within a voltage window of 4.8–2.0 V vs. Li/Li^+ (more details can be found in the experimental section). In our initial evaluation, GrPLMTOF200 exhibited the highest initial capacity (206 mAh g^{-1}) and stable cycling performance among the samples, suggesting that 200°C is the optimal annealing temperature for preserving the structural integrity of the DRX structure and graphene composite. Therefore, we selected GrPLMTOF200 for further electrochemical evaluations below. To evaluate the role of PEI in the self-assembly process, we also prepared a graphene-wrapped sample without the PEI (GrLMTOF200).

To understand the impact of solution-based graphene wrapping over LMTOF cathode particles, we used two control groups: (i) A carbon-LMTOF composite (LMTOF+C) prepared using high-energy dry ball-milling of LMTOF particles with 20 wt.% carbon additive (C65), which is the most frequently used in DRX research [3, 29, 30]. And (ii) LMTOF and graphene mixture (GrLMTOF200), which was prepared by mixing LMTOF and graphene in THF solvent without PEI coating over LMTOF. For performance comparison, GrPLMTOF200 and GrLMTOF200 electrodes were prepared with an additional 12 wt.% of C65 carbon additive to maintain the same total carbon content in the electrodes (20 wt.%) as the control group. Figure 4a presents the galvanostatic charge–discharge profiles of the GrPLMTOF200 at a current rate of 20 mA g^{-1} within a voltage window of 4.8–2.0 V vs. Li/Li^+. GrPLMTOF200 exhibited the characteristic sloped voltage profiles of DRX materials with an initial discharge capacity of 206 mAh g^{-1} at 20 mA g^{-1}, retaining 183 mAh g^{-1} after 100 cycles (Figure 4a) [1]. GrLMTOF200 also displays the DRX-like sloping profile, delivering 174 mAh g^{-1} initially and 148 mAh g^{-1} after 100 cycles (Figure S4). In contrast, LMTOF+C delivered a slightly higher initial discharge capacity of 235 mAh g^{-1} at 20 mA g^{-1}; however, only 147 mAh g^{-1} was maintained after 100 cycles (Figure 4b). The higher initial specific charge capacity in LMTOF+C is attributed to the smaller particle size generated during the high-energy dry milling process (Figure S5). Interestingly, the specific capacity of GrPLMTOF200 slightly increased from 206 to 220 mAh g^{-1} for the initial 16 cycles, which is attributed to the gradual transformation toward a delta phase [44]. This phase evolution is also confirmed by ex situ XRD of cycled GrPLMTOF200 electrodes (Figure S6), which reveals the presence of distinct spinel peaks consistent with prior reports of delta-phase transformation [45, 46]. The transformation is also evident from the evolution of the voltage profiles, which change

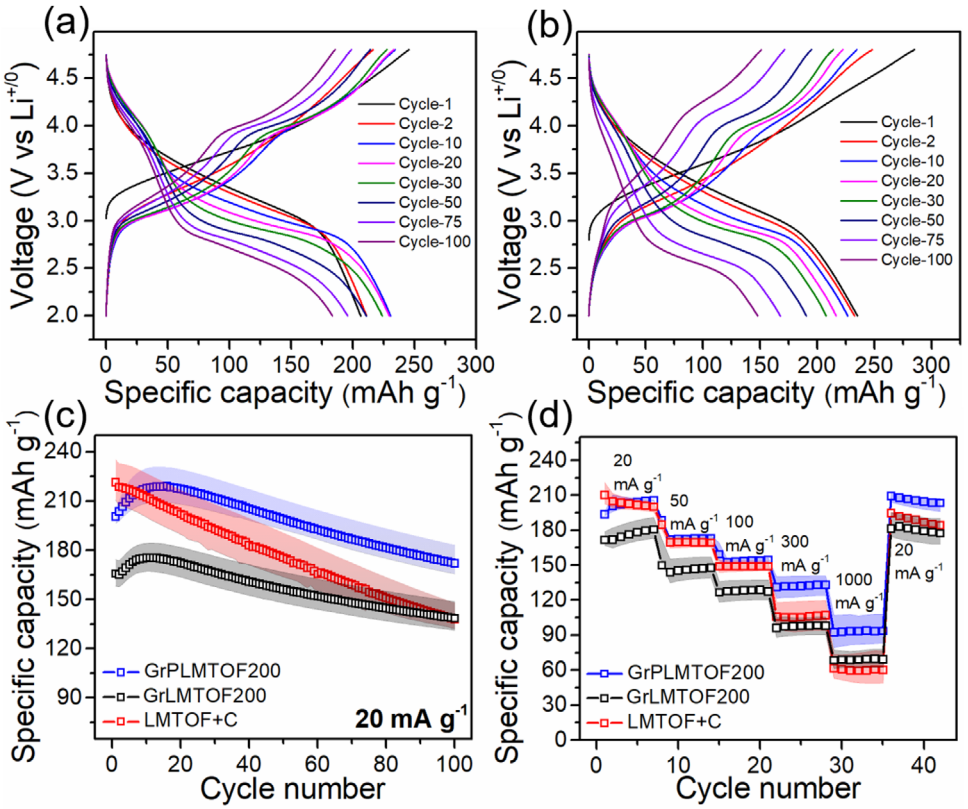

FIGURE 4 | Galvanostatic charge–discharge profiles of (a) GrPLMTOF200 and (b) LMTOF+C at a current density of 20 mA g^{-1}. (c) Cycling performance and (d) rate capability test of GrPLMTOF200, GrLMTOF200, and LMTOF+C.

from a sloped profile to the appearance of distinct plateaus at ~4.0 and ~3.0 V during cycling [46]. Such a delta-phase transformation in Mn-rich DRX compounds during electrochemical cycling is well documented [47, 48]. In contrast, this transformation was less pronounced in LMTOF+C. The rapid capacity decay in the ball-milled LMTOF+C likely superseded the capacity gain associated with the delta-phase transformation.

Figure 4c shows the cycling stability of GrPLMTOF200, GrLMTOF200, and LMTOF+C; the specific capacities were verified across three independently assembled coin cells under identical testing conditions. The plotted data represent the average values with associated minimum and maximum ranges. GrPLMTOF200 and GrLMTOF200 demonstrated superior cycling stability, retaining approximately 89% and 85% of their initial capacities after 100 cycles, respectively. In sharp contrast, LMTOF+C retains only 62%. Although the specific capacity retention of GrLMTOF200 is similar to that of GrPLMTOF200, GrLMTOF200 clearly shows a lower specific capacity, which is attributable to the difference in homogeneity of carbon distribution among the two samples. We further evaluated the rate capability of GrPLMTOF200 and GrLMTOF200 in comparison with LMTOF+C, as shown in Figure 4d and Figure S7. At low current densities (20 to 100 mA g^{-1}), GrPLMTOF200 and LMTOF+C exhibited similar discharge capacities while GrLMTOF200 showed lower capacities. However, GrPLMTOF200 clearly outperformed GrLMTOF200 and LMTOF+C at elevated current rates. For example, GrPLMTOF200 delivered a capacity of 92 mAh g^{-1} at 1000 mA g^{-1}, compared with 65 mAh g^{-1} for GrLMTOF200 and 61 mAh g^{-1} for LMTOF+C at 1000 mA g^{-1}. Direct-current (DC) polarization measurements were also conducted on LMTOF, GrPLMTOF200 and LMTOF+C powders without any additional carbon to evaluate their bulk electronic conductivity. The electronic conductivity of pristine LMTOF was measured to be 4.16×10^{-7} S cm^{-1}, whereas GrPLMTOF200 exhibited a dramatically higher conductivity of 4.56 S cm^{-1}, which is also higher than that of LMTOF+C (2.85 S cm^{-1}). These results provide direct evidence that graphene wrapping substantially improves electronic transport in the composite. Further, electrochemical impedance spectroscopy (EIS) measurements were performed on GrPLMTOF200, GrLMTOF200, and LMTOF+C after the first cycle, and the corresponding Nyquist plots are shown in Figure S8. GrPLMTOF200 exhibits the lowest charge-transfer resistance (42 Ω) compared to GrLMTOF200 (55 Ω) and LMTOF+C (162 Ω), clearly demonstrating the superior interfacial kinetics enabled by the solution-based graphene wrapping. In addition, EIS measurements collected after 10, 20, 30, 40, and 50 cycles reveal a much slower impedance growth for GrPLMTOF200 than for LMTOF+C, as shown in Figure S9. The charge-transfer resistance of GrPLMTOF200 evolves from 3 Ω after ten cycles to 20 Ω after 50 cycles, whereas LMTOF+C displays substantially higher values, increasing from 35 to 216 Ω over the same cycling interval. The lower resistance after ten cycles compared to the first cycle likely reflects early interfacial stabilization, while the subsequent gradual increase is associated with progressive interfacial aging during cycling. These results indicate that GrPLMTOF200 maintains a much more stable electrode-electrolyte interface, while LMTOF+C undergoes severe impedance growth during prolonged cycling. Collectively, these results confirm that

graphene wrapping significantly enhances both bulk electronic transport and interfacial charge-transfer kinetics, thereby improving rate performance and interfacial stability relative to conventional high-energy dry ball milling approaches. The specific contribution of the PEI layer to coating uniformity and interfacial stability is discussed in detail in the following section.

In an effort to reduce the amount of carbon additives in the LMTOF cathode composite, we fabricated and evaluated GrPLMTOF200 with varied super C65 carbon additive amounts (0, ~6.6, and ~12 wt.%) for comparison with LMTOF+C, as shown in Figure S10a. Although the GrPLMTOF200 with 12 wt.% additional carbon exhibited enhanced cycling performance, the composites with ~6.6 and 0 wt.% additional carbon also demonstrated excellent stability. GrPLMTOF200 (~6.6 wt.%) and GrPLMTOF200 (0 wt.%) retained 87.5% and 78% of their initial capacities after 100 cycles, respectively, whereas LMTOF+C showed only 62% retention. Despite having lower initial specific discharge capacities than LMTOF+C, the GrPLMTOF200 composites displayed significantly better long-term cycling stability with lower carbon contents. Figure S10b further compares the GrPLMTOF200 composites with 10 and 5 wt.% of graphene. Even with reduced graphene content, the composite maintained reasonable specific capacity and cycling stability, demonstrating the effectiveness of the graphene wrapping at lower loading.

Finally, the electrochemical performance of GrPLMTOF200 and LMTOF+C was evaluated in lithium-ion full-cells using graphite as the anode. Figure S11a, b shows the first charge–discharge profiles of the GrPLMTOF200 and LMTOF+C cathodes, together with the graphite anodes, cycled at 20 mA g^{-1} in the voltage ranges 4.8–2 V for the cathodes and 2–0.01 V for the graphite anode. Figure S11c,d compares the galvanostatic profiles of the LMTOF+C/graphite and GrPLMTOF200/graphite full-cells cycled at 20 mA g^{-1} at room-temperature in the voltage range of 2.0–4.6 V. The LMTOF+C/Graphite full-cell delivered first-cycle charge and discharge capacities of 193 and 141 mAh g^{-1}, respectively, and retained 118 mAh g^{-1} after the 30th cycle. In contrast, GrPLMTOF200/graphite full-cell delivered 183 and 156 mAh g^{-1} in the first cycle, and maintained 128 mAh g^{-1} after 30 cycles. Interestingly, in a full cell configuration, LMTOF+C showed a lower reversible capacity than GrPLMTOF200 in contrast to the Li-half cell system. We also observed much larger polarization and lower first-cycle Coulombic efficiency in the LMTOF+C/graphite full cell compared with the GrPLMTOF200/graphite full cell. These results indicate that graphene wrapping improves the cathode reversibility and enables more efficient full-cell operation.

2.4 | Importance of PEI Coating Layer to Synthesize Graphene-Wrapped Disordered Rock-Salt Oxides

To further understand the role of PEI coating in graphene composite synthesis, two graphene-wrapped LMTOF composites were synthesized with and without PEI coating on the LMTOF particles. Figure 5a presents an SEM image of the graphene-wrapped LMTOF composite without PEI coating. When the PEI coating layer was absent, the graphene wrapping over the LMTOF particles was incomplete. Many LMTOF particles remained unwrapped by graphene sheets (Figure 5b), and only a few regions of LMTOF particles were partially wrapped by graphene sheets (Figure 5c). To quantify the degree of graphene coverage, multiple SEM images collected from different regions of the sample were analyzed, and the number of LMTOF particles in direct contact with graphene sheets was compared with the total number of visible particles. Based on this image-based analysis, 31 out of 103 particles (~30%) in the sample prepared without PEI were directly connected to graphene. The unwrapped LMTOF particles appear with darker contrast and smoother morphology than the graphene-wrapped particles in Figure 5a. In addition, agglomerated graphene sheets without LMTOF particles were observed, as shown in the inset of Figure 5b. In contrast, the same statistical image analysis performed on the PEI-coated sample showed that 89 out of 101 particles (~88%) were associated with graphene sheets, indicating a much more homogeneous distribution when PEI was coated over the LMTOF surface (Figure 5d). Higher magnification images in Figure 5e,f further show that the graphene sheets are distributed over the LMTOF particle surfaces and confirm the more extensive graphene coverage in the PEI-coated sample. Moreover, SEM images in Figure S12, collected from multiple representative regions, further confirm that the enhanced graphene coverage is not localized but is, indeed, consistently observed throughout the sample. At higher magnification in Figure 5e,f, the PEI-coated LMTOF particles were further confirmed to be successfully wrapped by graphene sheets. These results demonstrate that the positively charged surface of LMTOF induced by PEI coating leads to a stronger attraction with the negatively charged graphene sheets. Moreover, the electrochemical performance of graphene-wrapped LMTOF composites with and without PEI coating is consistent with these morphological differences. As shown in Figure 4, the composite with PEI coating exhibits substantially improved performance relative to the composite without PEI coating, including higher initial coulombic efficiency (85% vs. 69%, Figure S13), higher specific capacity, superior rate capability, and lower charge-transfer resistance. These results collectively underscore the importance of the PEI coating on LMTOF particles in promoting effective electrostatic-attraction-driven self-assembly of graphene around LMTOF particles.

2.5 | Operando and Postmortem Analyses to Understand Improved Stability of Graphene-wrapped PEI-Coated Disordered Rock-Salt Oxides

To understand the improved electrochemical cycling stability of the GrPLMTOF200 positive electrodes compared with the conventionally prepared LMTOF positive electrodes (high-energy ball-milled with C65 carbon additive), operando and postmortem analyses were conducted after prolonged cycling. First, to quantify the irreversible oxygen (O_2) and carbon dioxide (CO_2) evolutions, differential electrochemical mass spectrometry (DEMS) measurements were performed on the LMTOF+C and GrPLMTOF200 electrodes. Figure 6a,b shows the voltage profiles along with the evolution of O_2 and CO_2 gases as a function of charge and discharge time. The LMTOF+C electrode (Figure 6a) exhibited significant O_2 evolution (4.6 mmol per mol LMTOF) at a voltage above 4.3 V, which agrees with previous reports on Mn-based DRX positive electrodes prepared by high-energy

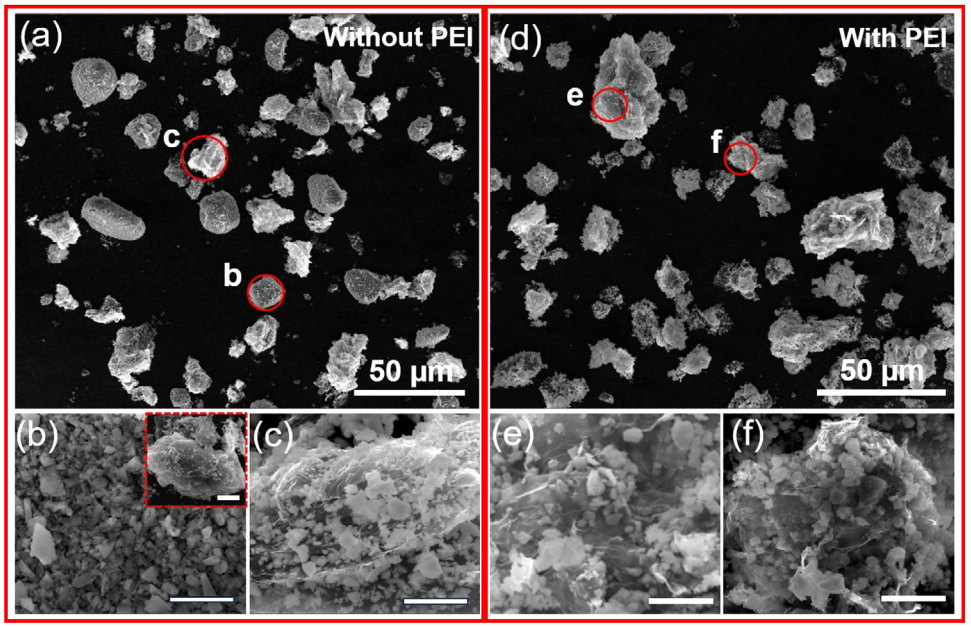

FIGURE 5 | SEM images of graphene-LMTOF composite (a–c) without PEI coating and (d–f) with PEI coating. The scale bars in b,c and e,f are 2 μm.

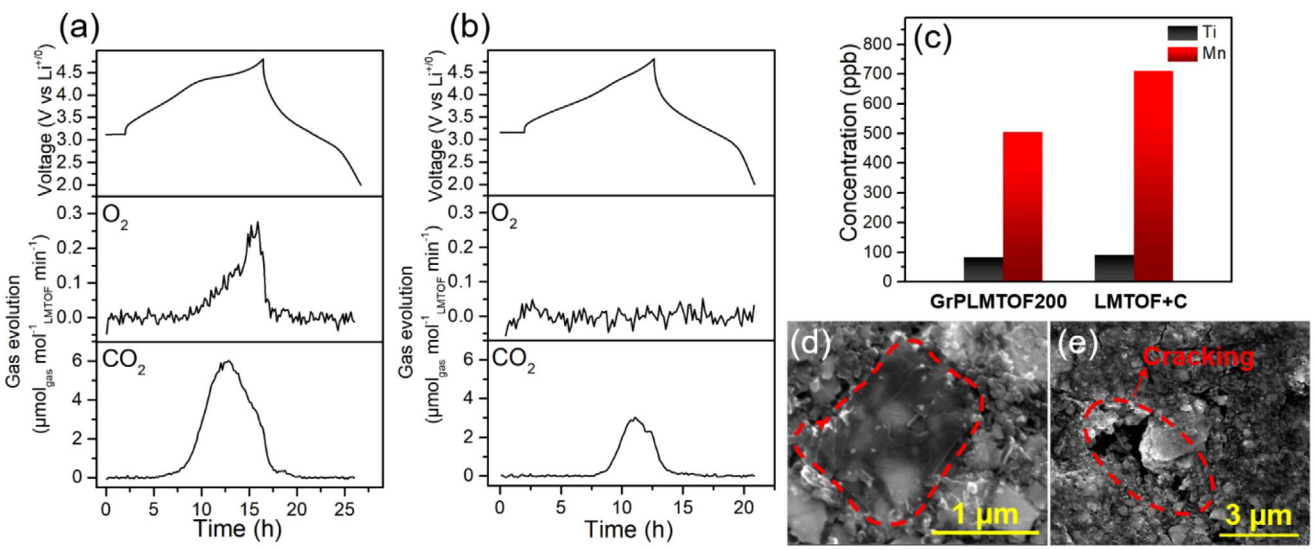

FIGURE 6 | DEMS analysis of O_2 and CO_2 gas evolution from (a) LMTOF+C and (b) GrPLMTOF200 cathodes during the first cycle. (c) ICP-MS of the separator extracted from the GrPLMTOF200 and LMTOF+C coin-cells after 50 cycles. SEM images of (d) GrPLMTOF200 and (e) LMTOF+C electrodes after 50 cycles at 20 mA g^{-1}.

ball milling [29, 49]. In contrast, GrPLMTOF200 (Figure 6b) showed no noticeable O_2 release throughout the charging process, demonstrating that the irreversible oxygen oxidation reaction is suppressed by graphene wrapping. This suppression is likely due to surface stabilization by graphene, which reduces reactive oxygen species and weakens direct electrolyte attack. Prior studies have shown that graphene-based surface layers can suppress oxygen loss by stabilizing surface oxygen [50, 51]. Moreover, the CO_2 evolution was also significantly reduced in GrPLMTOF200 compared with LMTOF+C (173.4 vs. 60.9 mmol per mol LMTOF, respectively), indicating enhanced interfacial stability [52, 53]. The simultaneous suppression of both O_2 and CO_2 evolution suggests that graphene wrapping mitigates not only lattice-oxygen instability but also electrolyte decomposition at the cathode interface.

Further, the XPS C1s and O1s spectra of the cycled GrPLMTOF200 and LMTOF+C electrodes revealed distinct features in surface oxygen species, as shown in Figure S14. After 50 cycles, the GrPLMTOF200 electrode (Figure S14a,b) exhibited a relatively stronger M—O peak at 529.7 eV, indicating improved preservation of lattice oxygen. In contrast, the LMTOF+C electrode (Figure S14c,d) showed a diminished M—O peak together with more pronounced signals at ~531.8 and ~533 eV, corresponding to

oxygenated surface species [37, 54]. Quantitative fitting of the O 1s and C 1s spectra further supports this interpretation. In particular, the relative contribution of lattice M—O species is higher for GrPLMTOF200 (~21%) than for LMTOF+C (~11%) after 50 cycles, whereas oxygenated/carbonate-related surface components are more pronounced in LMTOF+C (~52%) compared with the graphene-wrapped sample (~40%). These results indicate the formation of a thinner and less degraded CEI layer in GrPLMTOF200. Thus, the post-cycling XPS results are consistent with the DEMS measurements and together support that graphene wrapping suppresses oxygen-related surface degradation and parasitic interfacial reactions. Overall, these findings illustrate that the LMTOF+C electrode underwent more severe surface degradation and parasitic side reactions, underscoring the effectiveness of graphene wrapping in suppressing interfacial degradation in the DRX electrodes. Our observation of suppressed O_2/CO_2 evolution in the graphene-wrapped LMTOF is also consistent with previous theoretical and mechanistic studies on graphene-oxide interfaces [55, 56]. These insights support our interpretation that the graphene-wrapped surface in the present work stabilizes lattice oxygen and suppresses oxygen-loss-driven degradation.

TM dissolution of the cathode active material in a liquid electrolyte is another important cause of performance degradation [57–60]. To investigate TM dissolution of GrPLMTOF200 and LMTOF+C composites in electrolytes, inductively coupled plasma mass spectroscopy (ICP-MS) analysis was performed on separators extracted after 50 charge–discharge cycles at 20 mA g^{-1}. Figure 6c shows the Mn and Ti concentrations detected in the separators after 50 cycles when GrPLMTOF200 and LMTOF+C electrodes were used. When the GrPLMTOF200 electrode was used, 500 ppb of Mn and 80 ppb of Ti were observed. In contrast, higher concentrations of both Mn (710 ppb) and Ti (90 ppb) were detected when using the LMTOF+C electrode. These results indicate that the graphene wrapping suppresses Mn and Ti dissolution during battery cycling.

Lastly, we examined the morphological evolution of the cycled GrPLMTOF200 and LMTOF+C electrodes after 50 cycles at 20 mA g^{-1} using SEM, as shown in Figure 6d,e. The GrPLMTOF200 electrode retained graphene wrapping over the LMTOF particles even after extended cycling, and no visible large gaps between graphene and LMTOF particles were found (Figure 6d). These results indicate that the graphene wrapping is mechanically robust, which mitigates contact loss between conductive carbon and LMTOF particles. In contrast, the LMTOF+C electrode exhibited noticeable cracking after 50 cycles, signifying the mechanical instability of the carbon-LMTOF contact. Similar cracking behaviors in DRX electrodes were previously reported when the electrodes were prepared by high-energy ball milling with conductive carbon additives [61]. This sharp contrast between the two samples highlights the impact of graphene wrapping in improving the structural integrity of the electrodes.

3 | Discussion

DRX compounds are considered an important class of cathode materials as they combine low cost through the use of earth-abundant elements with high-energy density at the material level. However, high-energy ball milling (or shaker milling) and a substantial amount of carbon additives are required for DRX compounds to deliver high specific capacities and reasonable rate capabilities [7, 9, 12, 17, 19, 21]. In a typical DRX positive-electrode preparation in the literature, DRX active materials are subject to high-energy ball milling or shaker milling with ~20 wt.% conductive carbon additives [3, 9, 11, 12, 17, 19, 21, 62]. The milling process pulverizes the DRX particles, which promotes Li diffusion [2]. However, this additional milling process increases the surface area and can even create surface defects. The increased surface area and surface defects formed by the milling process promote unwanted side reactions, including electrolyte decomposition and TM dissolution. Furthermore, insufficient carbon loading or non-uniform carbon distribution can lead to an incomplete electronic percolation network, causing spatially heterogeneous current distribution and overpotential-induced overcharging of poorly connected particles. Such localized overcharging is well known to accelerate structural degradation in low-conductivity cathodes [63, 64]. All of these factors degrade the cycling performance of DRX cathodes, which remains a critical challenge. In addition, the use of a substantial amount of conductive carbon additives, typically 20 wt.% or sometimes even higher, reduces the electrode-level capacity and energy density [2].

Figure 7a summarizes the properties of Mn-based DRX cathodes in terms of active material portion in the electrode, capacity retention after 50 cycles, and the first discharge capacity [7, 9, 12, 17, 19–21, 61]. In this analysis, previous literature that provides stability test results for at least 50 cycles was included. As shown in Figure 7a, most of the reports contain ~20 wt.% of additive carbon and, therefore, ~70 wt.% of active material in the electrode. A few studies applied lower carbon additives in the DRX electrode; however, they still required high-energy dry ball milling or a shaker milling process for mixing with carbon additives or creating a carbon coating [19, 20, 61]. Although graphene wrapping was successfully applied over DRX particles without the milling process with high specific capacity in the first discharge in our previous work, the aqueous-solution-based synthesis process resulted in TM dissolution and Li^+/H^+ exchange, contributing to cycling performance degradation [7].

In contrast, in the current work, we developed graphene-wrapped DRX particles without such undesired reactions by screening potential processing solvent candidates and selecting a non-aqueous and moderately polar solvent (THF). Compared to previous reports, GrPLMTOF200, which was developed in this study, exhibited improved cycling stability when 70 wt.% active material loading was used. Even with 9 wt.% of carbon (81 wt.% active material loading), GrPLMTOF200 could retain ~93% of the initial discharge capacity after 50 cycles. Impressively, GrPLMTOF200 (with 20 wt.% total carbon) exhibited a much lower capacity decay rate (0.11% decay per cycle) than recently reported Mn-based DRX cathodes employing ball-milled carbon, graphitic carbon coatings, pyrolysis-derived carbon coatings, and other carbon-modified strategies, as summarized in Figure 7b [7, 9, 12, 17, 19–21, 61]. Although the reduced carbon content in the GrPLMTOF200 cathode resulted in increased capacity decay rates, likely due to incomplete carbon coverage, these rates remained superior to those of many Mn-based DRX cathodes

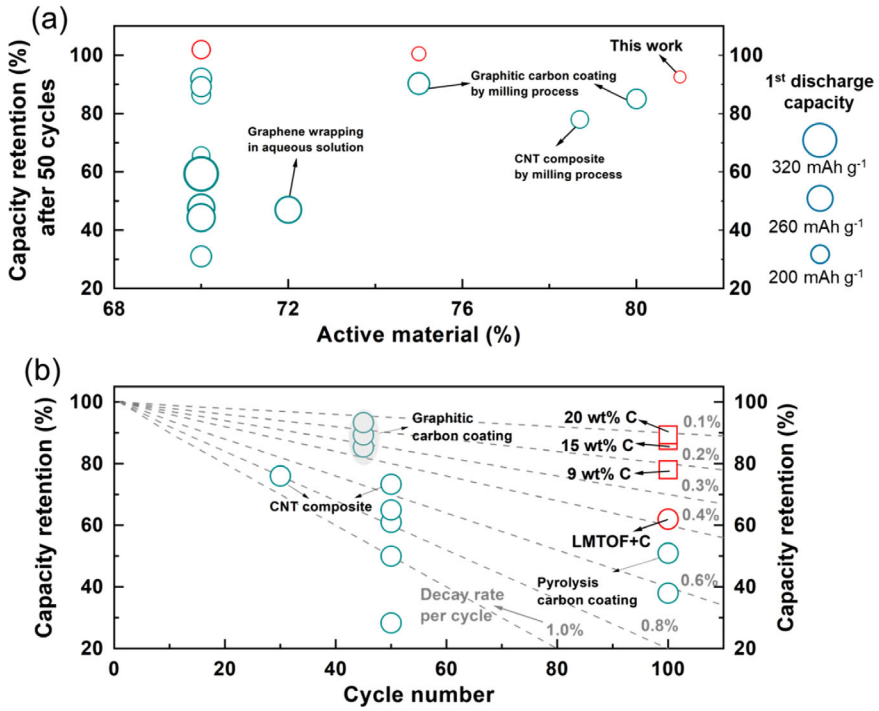

FIGURE 7 | (a) Performance summary of Mn-based DRX cathodes in active material (wt.%) in electrodes vs. capacity retention (%) after 50 cycles. Only previous literature findings that provided stability test results for at least 50 cycles were included in this analysis [7, 9, 12, 17, 19–21, 61]. The size of the circles shows the first discharge capacity. (b) Capacity retention of Mn-based DRX compounds. The red squares represent GrPLMTOF200 cathodes, and the red circle represents the LMTOF+C cathode. The gray dashed lines represent the capacity decay rate per cycle.

with similar or higher carbon contents. The improved cycling performance is attributable to the following factors: (i) Our solution-based graphene wrapping approach eliminates the need for high-energy dry ball milling step while achieving high specific capacity. Although our approach still uses a wet ball milling process to reduce the particle size to several hundred nanometers, the wet ball milling process is known to be a less energy intensive and milder process. In contrast, the traditional high-energy dry ball milling process creates surface defects and reduces the particle size to sub-hundred nanometers that can accelerate the undesired side reactions at the particle surface. (ii) The robust graphene wrapping provides an electron transport network throughout the electrode. (iii) The graphene wrapping suppresses unwanted side reactions such as electrolyte decomposition, lattice oxygen evolution, and TM dissolution by protecting the DRX surface. Although our approach significantly improves the cycling performance of Mn-based DRX cathodes, it is still necessary to further reduce the carbon loading (< 9 wt.%) in the electrode without compromising performance to make the DRX practically viable.

4 | Conclusion

In this work, we demonstrated a non-aqueous, solution-based coating approach to fabricate graphene-wrapped $Li_{1.2}Mn_{0.6}Ti_{0.2}O_{1.8}F_{0.2}$ (LMTOF) cathodes using electrostatic-attraction-driven self-assembly followed by low-temperature heat treatment. This strategy circumvents the limitations of conventional ball-milling processes and aqueous processing by preserving the structural integrity of the DRX framework while enabling uniform graphene wrapping. The resulting GrPLMTOF200 composite exhibited superior cycling stability and improved rate capability compared with a conventionally prepared ball-milled carbon-LMTOF composite. Postmortem analysis confirmed the suppressed oxygen evolution, reduced parasitic reactions, lower TM dissolution, and retention of graphene wrapping after extended cycling. These results suggest that graphene wrapping not only improves electronic connectivity but also stabilizes the cathode surface against oxygen-related degradation. Overall, this work highlights the effectiveness of solution-processed carbon wrapping in stabilizing DRX cathodes and suggests a scalable path for high-capacity lithium-ion battery materials.

5 | Experimental Section

5.1 | Material Synthesis

LMTOF was prepared via solid-state synthesis following a previously reported synthesis procedure [36]. Mn_2O_3, TiO_2, Li_2CO_3, and LiF precursors were used to synthesize the targeted DRX compound of $Li_{1.2}Mn_{0.6}Ti_{0.2}O_{1.8}F_{0.2}$. Mn_2O_3 (30 mol.%), TiO_2 (20 mol.%), Li_2CO_3 (50 mol.%), and LiF (20 mol.%) precursors, with a total mass of ~200 g, were ball-milled together with Y-stabilized ZrO_2 in 500 mL jars at 100 rpm using a Retsch planetary ball mill PM 400 for 12 h. The milled precursors were calcined at 900°C for 12 h using a ramp rate of 5°C min^{-1} under an argon (Ar) atmosphere. Calcination was performed as a loose powder in 20 g batches. Multiple batches of the calcined DRX material, totaling 90 g, were subsequently ball-milled together at 400 rpm in an organic solvent for 4 h without any carbon. The ball-milled

material was recovered, dried, and sieved using a 45-micron mesh. The Li, Mn, Ti, and F contents of the pristine DRX powder were determined using ICP-OES and F-ISE, with the results listed in Table S1. All the processes and pristine materials analysis were conducted at the Argonne National Laboratory (ANL) Materials Engineering Research Facility (MERF) facility.

For the graphene-wrapped PEI-coated LMTOF (GrPLMTOFP) synthesis, LMTOF particles were first coated by PEI, following the procedure described in our previous work [7]. Initially, 10 wt.% of graphene (MSE supplies) was dispersed in THF (Sigma–Aldrich, 99.9%) and sonicated for 60 min. Subsequently, 90 wt.% of the PEI-coated LMTOF powder was added to the dispersed graphene solution. The suspension was sonicated for 15 min and then stirred for 15 min at room-temperature to promote uniform graphene wrapping through electrostatic interaction. The composite was obtained by washing the suspension with THF solvent, followed by drying at 70°C. The as-prepared GrPLMTOFP composite was then subjected to heat treatment at different temperatures (200°C, 300°C, and 400°C) under Ar flow for 2 h to remove the residual surface functional groups (heating rate of 5°C min^{-1}). For the synthesis of GrLMTOF control groups, the composite was prepared by adding LMTOF particles to the graphene dispersion without PEI coating. For the LMTOF+C composite, 280 mg of the as-synthesized LMTOF cathodes and 80 mg of super C65 carbon black (Timcal) were mixed using shaker milling for 1 h using a SPEX8000M mill.

5.2 | Materials Characterization

The zeta potential was collected on a NanoBrook 90Plus PALS from Brookhaven Instruments. Each powder sample was dispersed individually in the selected solvents (THF, NMP, DMF, and EG) to create a starting stock suspension. The powder was added to 2.5 mL of the solvent to obtain a 5 wt.%. Then, 20 μL of the starting stock suspension was added to a separate tube filled with 10 mL of the same selected solvent to create the dilute measurable suspension. Phase analysis light scattering (PALS) mode was utilized for the zeta potential measurements. Each reported value represents the average of 100 cycles for each material. Inductively coupled plasma mass spectroscopy (ICP-MS; Agilent 7900) was used to determine the concentration of each element present in the processing solution. For these measurements, 20 mg of LMTOF was dispersed in 20 mL of THF, NMP, DMF, and EG solvents for 24 h. For the analysis, 20 μL of the solution was collected after filtering out the LMTOF and then diluted with 5% nitric acid for the ICP-MS analysis. For the post-cycling measurement, the separators from the cycled cells were collected and dried in a vacuum chamber before dispersing them in diluted nitric acid [65]. The calibration curve was generated using standard solutions with five different concentrations ranging from 1 to 1000 ppb. Linear fitting was applied.

A Rigaku Miniflex 600 high-resolution diffractometer equipped with a Cu-Kα source (λ = 0.15418 nm) was used for recording the XRD patterns of the LMTOF-based samples. Microstructural analysis of the LMTOF samples was conducted using a FEI Quanta FEG-250 and Phenom PW-100-017 scanning electron microscope. EDS elemental mappings were recorded using a Bruker Quantax EDS detector. The graphene content in the GrPLMTOF composite was estimated using a ThermoFisher Flash Smart Elemental Analyzer, which performs C, H, N, and S analysis with a detection limit of 0.01%. A Kratos Axis Ultra equipped with a monochromated aluminum source (Kα = 1486.6 eV) was used for collecting the X-ray photoelectron spectra. Survey spectra were obtained using a pass energy of 160 eV. High-resolution, core-level spectra for all the elements were obtained using a pass energy of 20 eV. All the spectra were referenced against the C1s peak at 284.5 eV to compensate for charging effects during acquisition. Quantitative analysis was performed based on the integrated peak area of each fitted component. The reported percentages therefore represent the relative fitted area of each XPS component and reflect the fraction of different surface species present on the electrode surface. Raman analysis was performed using a Renishaw PLC Raman spectrometer equipped with a 532 nm laser in the range of 900–4000 cm^{-1}.

For the operando gas measurements, a custom-built setup and gas-tight cell were used, which have been described in detail in a previous publication [66]. Custom Swagelok cells were assembled inside an Ar-filled glovebox as follows: a lithium-foil disc (12 mm ⌀), a quartz microfiber separator (Whatman, QM-A; 12.7 mm ⌀) wetted with 80 μL of electrolyte solution, a GrPLMTOF200 or LMTOF+C electrode on stainless-steel mesh current collector (12 mm ⌀), a stainless-steel mesh disc (12 mm ⌀), and a stainless-steel ring spacer (12 mm ⌀) were compressed inside a modified Swagelok cell. The spacer ring creates a headspace (~100 μL) for gases to accumulate during battery operation. 1 M $LiPF_6$ (Gotion) in EC/DMC (1:1 v/v; both Gotion) was used as the electrolyte solution.

After assembly, the GrPLMTOF/Li and LMTOF+C/Li cells were connected to the DEMS equipment, and the headspace of the cell was filled with a positive Ar pressure (~1.45 bar). During the electrochemical measurements, the cell headspace was flushed with 500 μL of argon by the DEMS instrument every 10 min, and any accumulated gases were swept to the mass spectrometer chamber for analysis. The mass spectrometer was calibrated for O_2 (research grade, Linde) and CO_2 (> 99.9%, Linde), allowing for the conversion of the ion current to partial pressure for O_2 and CO_2, which could then be used to quantify gas formation using the ideal gas law (temperature and volume are known).

Electrochemical measurements were performed at 25°C using a Biologic VSP potentiostat/galvanostat instrument running EC-lab software. After a 2 h OCV period to establish a baseline value for all mass traces, the cells were cycled between 4.8 and 1.5 V_{Li}. Charging and discharging were performed at 20 mA g^{-1} in constant current (CC) mode.

5.3 | Electrochemical Study

Graphene-wrapped PEI-coated LMTOF composite electrodes were prepared by hand mixing 78 wt.% GrPLMTOF with 12 wt.% super C65 (Timcal) and 10 wt.% polytetrafluoroethylene (PTFE, DuPont, Teflon 8A). For the LMTOF+C composite, 70 wt.% LMTOF was shaker milled with 20 wt.% of C65, and the electrode was prepared by mixing 90 wt.% of the resulting composite and 10 wt.% of PTFE binder. The mixed composites were then rolled into ~40 μm free-standing thin films inside an Ar-filled glovebox.

Coin-type 2032 two-electrode cells were fabricated using the composite working electrode (10 mm diameter) containing ~2.5 mg cm^{-2} of the active material, a Li-foil counter electrode, and a glass fiber separator (Whatman, GF/F type). The electrolyte consisted of a 1 M solution (99.99%, Solvionic) of $LiPF_6$ in a 1:1 mixture of ethylene carbonate (EC) and dimethyl carbonate (DMC). A glove box (VAC) filled with high-purity argon (99.999%) and equipped with oxygen and moisture sensors/absorbers (H_2O and O_2 content < 1 ppm) was used for assembling the electrochemical cells. Li-ion half-cells were subjected to galvanostatic long-term cycling at 20 mA g^{-1} in the voltage range of 4.8–2 V using an Arbin battery test instrument at room temperature. Three individual cells were tested for each sample for the electrochemical measurements.

The coin-type full-cells were assembled with LMTOF-based cathodes and graphite as the anode, with a glass fiber separator (Whatman, GF/D type) and 1 M LiPF6 in EC/DMC electrolyte. The composite graphite electrodes were fabricated as described in our previous work [30]. Li-ion full cells were optimized by balancing the N/P ratio (~1.1), where N corresponds to the graphite discharge capacity and P to the charge capacity of the LMTOF-based cathode. Galvanostatic cycling of the full cells was carried out at a current density of 20 mA g^{-1} within a voltage range of 2.0–4.6. The current density and specific capacity values for the full cells are based on the cathode active material mass.

The electronic conductivity of LMTOF, LMTOF+C, and 10GrPLMTOF powders was determined by the DC polarization method. A carbon-coated Al/cathode powder/carbon-coated Al blocking-cell configuration in a Wellcos cell was used for the measurements, with a powder thickness of ~50 μm. The conductivity measurements were carried out using a VMP-300 BioLogic potentiostat under a stacking pressure of 75 MPa. Constant voltages of 0.01, 0.02, 0.03 and 0.05 V were each applied for 30 min, and the steady-state current at each potential was recorded. The average steady-state current at each applied voltage was then used to calculate the electronic conductivity according to $\sigma = L / (R.A)$, where L is the thickness of the powder layer, R is the resistance, and A is the electrode area. The resistance, R, was obtained from the applied voltage and measured current (Figure S15).

5.4 | Sample Preparation for Postmortem Analysis

For the postmortem studies, the coin-cells containing GrPLMTOF200 and LMTOF+C electrodes were cycled at 20 mA g^{-1} in the voltage range of 4.8–2.0 V for 50 cycles. After cycling, the cells were disassembled inside the Ar-filled glovebox, and the electrodes and separators were removed. The electrodes were rinsed with 200 μL of dimethyl carbonate (DMC) and then dried in a vacuum chamber before performing post-cycling studies.

Author Contributions

V.S.A. and H.K. conceived the concept of this study. M.Z. and I.S.B. synthesized the LMTOF under the supervision of O.K. V.S.A. synthesized the composite materials and conducted materials characterization and electrochemical measurements. B.L.A. performed the zeta potential measurements. S.W. conducted the ICP-MS analysis. F.B. and H.L. performed and analyzed the XPS measurements. M.X.T. conducted Raman measurements under the supervision by R.K. B.L.D.R. conducted DEMS analysis, supervised by B.D.M. V.S.A. and Y. F prepared and conducted full cell testing, supervised by V. B. V.S.A. and H.K. wrote the original draft. All the authors reviewed and edited the manuscript.

Acknowledgements

This work was supported by the Assistant Secretary for Energy Efficiency and Renewable Energy, Transportation Technologies Office, of the U.S. Department of Energy under Contract DEAC02-05CH11231 (DRX+ program). This work used resources affiliated with the Liquid Sunlight Alliance, which is supported by the U.S. Department of Energy, Office of Science, Office of Basic Energy Sciences, Fuels from Sunlight Hub under Award Number DE-SC0021266T. The authors utilized ChatGPT to assist with grammar correction, language polishing, and enhancing the overall coherence. They carefully reviewed and edited all the content to guarantee its accuracy and originality, and they take full responsibility for the final version of the publication.

Conflicts of Interest

The authors declare no conflicts of interest.

Data Availability Statement

The data that support the findings of this study are available from the corresponding author upon reasonable request.

References

1. R. Clément, Z. Lun, and G. Ceder, "Cation-Disordered Rocksalt Transition Metal Oxides and Oxyfluorides for High Energy Lithium-Ion Cathodes," *Energy & Environmental Science* 13 (2019): 345–373.

2. H. Li, R. Fong, M. Woo, et al., "Toward High-Energy Mn-Based Disordered-Rocksalt Li-Ion Cathodes," *Joule* 6 (2022): 53–91, https://doi.org/10.1016/j.joule.2021.11.005.

3. Z. Lun, B. Ouyang, D. H. Kwon, et al., "Cation-Disordered Rocksalt-Type High-Entropy Cathodes for Li-Ion Batteries," *Nature Materials* 20 (2021): 214–221, https://doi.org/10.1038/s41563-020-00816-0.

4. D. Chen, J. Ahn, and G. Chen, "An Overview of Cation-Disordered Lithium-Excess Rocksalt Cathodes," *ACS Energy Letters* 6 (2021): 1358–1376, https://doi.org/10.1021/acsenergylett.1c00203.

5. R. Chen, C. L. A. Leung, and C. Huang, "Exploring the Properties of Disordered Rocksalt Battery Cathode Materials by Advanced Characterization," *Advanced Functional Materials* (2024): 2308165, https://doi.org/10.1002/adfm.202308165.

6. M. Wang, X. Chen, H. Yao, et al., "Research Progress in Lithium-Excess Disordered Rock-Salt Oxides Cathode," *Energy & Environmental Materials* 5 (2022): 1139–1154, https://doi.org/10.1002/eem2.12413.

7. V. S. Avvaru, M. Zuba, B. L. Armstrong, et al., "Aqueous Solution-Based Synthesis Approach for Carbon-Disordered Rocksalt Composite Cathode Development and Its Limitations," *Electrochimica Acta* 509 (2025): 145302, https://doi.org/10.1016/j.electacta.2024.145302.

8. R. Fong, N. Mubarak, S. W. Park, et al., "Redox Engineering of Fe-Rich Disordered Rock-Salt Li-Ion Cathode Materials," *Advanced Energy Materials* (2024): 2400402, https://doi.org/10.1002/aenm.202400402.

9. S. Patil, D. Darbar, E. C. Self, et al., "Alternate Synthesis Method for High-Performance Manganese Rich Cation Disordered Rocksalt Cathodes," *Advanced Energy Materials* 13 (2023): 2203207, https://doi.org/10.1002/aenm.202203207.

10. H. Lee, M. Kim, H. Park, et al., "Stabilization of Oxygen-Dependent $Fe^{3+}/^{4+}$ Redox in Li-Excess DRX Cathode Exhibiting Anionic Redox via Transition Metal Combination," *Advanced Functional Materials* 34 (2024): 2312401, https://doi.org/10.1002/adfm.202312401.

11. F. Liu, J. He, H. Chen, W. Yang, R. Yu, and Z. Lun, "Design Principles for High-Capacity, Long-Life Cation-Disordered Rocksalt Cathodes," *Advanced Functional Materials* 35 (2025): 2419907, https://doi.org/10.1002/adfm.202419907.

12. V. C. Wu, H. A. Evans, R. Giovine, et al., "Rapid and Energy-Efficient Synthesis of Disordered Rocksalt Cathodes," *Advanced Energy Materials* 13 (2023): 2203860, https://doi.org/10.1002/aenm.202203860.

13. J. Qian, Y. Ha, K. P. Koirala, et al., "Toward Stable Cycling of a Cost-Effective Cation-Disordered Rocksalt Cathode via Fluorination," *Advanced Functional Materials* 33 (2023): 2205972, https://doi.org/10.1002/adfm.202205972.

14. J. Ahn, D. Chen, and G. Chen, "A Fluorination Method for Improving Cation-Disordered Rocksalt Cathode Performance," *Advanced Energy Materials* 10 (2020): 2001671, https://doi.org/10.1002/aenm.202001671.

15. Z. Zhang, J. Liu, P. H. Du, D. Xia, and Q. Sun, "Screening Na-Excess Cation-Disordered Rocksalt Cathodes with High Performance," *ACS Nano* 18 (2024): 30584–30592.

16. A. Outka, H. P. Ho, W. C.-H. Kuo, et al., "Electron Localization in Cation-Disordered Rock Salt Electrodes," *ACS Energy Letters* 9 (2024): 1863–1870, https://doi.org/10.1021/acsenergylett.4c00264.

17. H. Ahmed, M. Woo, N. Dumaresq, et al., "Nucleation-Promoting and Growth-Limiting Synthesis of Disordered Rock-Salt Li-Ion Cathode Materials," *Nature Communications* 16 (2025): 5806, https://doi.org/10.1038/s41467-025-60946-4.

18. E. C. M. Barbosa, J. Du, A. S. Pal, A. Kondrakov, and T. Brezesinski, "Optimizing Disordered Rock Salt Cathodes by Solid-State Synthesis and Design of Experiments for Enhanced Battery Performance," *Advanced Sustainable Systems* 9 (2025): 2400931, https://doi.org/10.1002/adsu.202400931.

19. J. Xu, S. Patil, K. P. Koirala, et al., "Enhancing the Electrode Gravimetric Capacity of $Li_{1.2}Mn_{0.4}Ti_{0.4}O_2$ Cathode Using Interfacial Carbon Deposition and Carbon Nanotube-Mediated Electrical Percolation," *ACS Applied Materials & Interfaces* 15 (2023): 31711–31719, https://doi.org/10.1021/acsami.3c04805.

20. S. Patil, K. P. Koirala, M. J. Crafton, et al., "Enhanced Electrochemical Performance of Disordered Rocksalt Cathodes Enabled by a Graphite Conductive Additive," *ACS Applied Materials & Interfaces* 15 (2023): 39253–39264, https://doi.org/10.1021/acsami.3c05619.

21. Y. Zhou, Y. Xu, J. Song, and Q. Tan, "Preparation and Performance Investigation of Carbon-Coated $Li_{1.2}Mn_{0.2}Ti_{0.6}O_2$/C Cathode Materials," *ACS Applied Materials & Interfaces* 16 (2024): 52539–52549, https://doi.org/10.1021/acsami.4c12757.

22. C. Hu, K. Lin, X. Wang, et al., "Electrostatic Self-Assembling Formation of Pd Superlattice Nanowires From Surfactant-Free Ultrathin Pd Nanosheets," *Journal of the American Chemical Society* 136 (2014): 12856–12859, https://doi.org/10.1021/ja507409p.

23. M. Karayianni and S. Pispas, "Block Copolymer Solution self-Assembly: Recent Advances, Emerging Trends, and Applications," *Journal of Polymer Science* 59 (2021): 1874–1898, https://doi.org/10.1002/pol.20210430.

24. H. P. Cong and S. H. Yu, "Self-Assembly of Functionalized Inorganic–Organic Hybrids," *Current Opinion in Colloid & Interface Science* 14 (2009): 71–80, https://doi.org/10.1016/j.cocis.2008.09.003.

25. K. Lobo, P. R. Sumbe, M. A. More, D. J. Late, and H. S. S. R. Matte, "Solution-Based Electrostatic Self-Assembly Route for Obtaining Graphene–Transition Metal Dichalcogenide Heterostructures," *Dalton Transactions* 53 (2024): 3465–3469, https://doi.org/10.1039/D3DT03749E.

26. H. Kim, K. Y. Park, M. Y. Cho, et al., "High-Performance Hybrid Supercapacitor Based on Graphene-Wrapped $Li_4Ti_5O_{12}$ and Activated Carbon," *ChemElectroChem* 1 (2014): 125–130, https://doi.org/10.1002/celc.201300186.

27. N. I. Nungu, K. J. Nyamtara, N. C. Karima, et al., "Facile Synthesis Method of Self-Assembled Ni-Rich $LiNi_{0.8}Mn_{0.1}Co_{0.1}O_2$/rGO Composite for High-Performance Li-Ion Batteries," *International Journal of Energy Research* 2024 (2024): 5663332, https://doi.org/10.1155/2024/5663332.

28. J. H. Shim, Y. M. Kim, M. Park, J. Kim, and S. Lee, "Reduced Graphene Oxide-Wrapped Nickel-Rich Cathode Materials for Lithium Ion Batteries," *ACS Applied Materials & Interfaces* 9 (2017): 18720–18729, https://doi.org/10.1021/acsami.7b02654.

29. J. Ahn, Y. Ha, R. Satish, et al., "Exceptional Cycling Performance Enabled by Local Structural Rearrangements in Disordered Rocksalt Cathodes," *Advanced Energy Materials* 12 (2022): 2200426, https://doi.org/10.1002/aenm.202200426.

30. V. S. Avvaru, T. Li, G. H. Lee, et al., "Alternative Solid-State Synthesis Route for Highly Fluorinated Disordered Rock-Salt Cathode Materials for High-Energy Lithium-Ion Batteries," *Advanced Energy Materials* 15 (2025): 2500492, https://doi.org/10.1002/aenm.202500492.

31. C. Pramanik, J. R. Gissinger, S. Kumar, and H. Heinz, "Carbon Nanotube Dispersion in Solvents and Polymer Solutions: Mechanisms, Assembly, and Preferences," *ACS Nano* 11 (2017): 12805–12816, https://doi.org/10.1021/acsnano.7b07684.

32. D. H. Gharib, F. Malherbe, and S. E. Moulton, "Debundling, Dispersion, and Stability of Multiwalled Carbon Nanotubes Driven by Molecularly Designed Electron Acceptors," *Langmuir* 34 (2018): 12137–12144, https://doi.org/10.1021/acs.langmuir.8b02878.

33. D. W. Johnson, B. P. Dobson, and K. S. Coleman, "A Manufacturing Perspective on Graphene Dispersions," *Current Opinion in Colloid & Interface Science* 20 (2015): 367–382, https://doi.org/10.1016/j.cocis.2015.11.004.

34. J. I. Paredes, S. Villar-Rodil, A. Martínez-Alonso, and J. M. D. Tascón, "Graphene Oxide Dispersions in Organic Solvents," *Langmuir* 24 (2008): 10560–10564, https://doi.org/10.1021/la801744a.

35. T. C. de Oliveira, F. V. Ferreira, B. R. C. de Menezes, et al., "Engineering the Surface of Carbon-Based Nanomaterials for Dispersion Control in Organic Solvents or Polymer Matrices," *Surfaces and Interfaces* 24 (2021): 101121.

36. R. A. Ahmed, K. P. Koirala, G. H. Lee, et al., "Enhanced Electrochemical Performance of Disordered Rocksalt Cathodes in a Localized High-Concentration Electrolyte," *Advanced Energy Materials* 14 (2024): 2400722, https://doi.org/10.1002/aenm.202400722.

37. H. Kim, K. Y. Park, J. Hong, and K. Kang, "All-Graphene-Battery: Bridging the Gap Between Supercapacitors and Lithium Ion Batteries," *Scientific Reports* 4 (2014): 5278, https://doi.org/10.1038/srep05278.

38. F. T. Johra, J. W. Lee, and W. G. Jung, "Facile and Safe Graphene Preparation on Solution Based Platform," *Journal of Industrial and Engineering Chemistry* 20 (2014): 2883–2887, https://doi.org/10.1016/j.jiec.2013.11.022.

39. S. Stankovich, D. A. Dikin, R. D. Piner, et al., "Synthesis of Graphene-Based Nanosheets via Chemical Reduction of Exfoliated Graphite Oxide," *Carbon* 45 (2007): 1558–1565, https://doi.org/10.1016/j.carbon.2007.02.034.

40. Y. Wang, S. Huang, B. Raji-Adefila, A. Outka, J. H. Wang, and D. Chen, "Unraveling the Nature and Role of Layered Cation Ordering in Cation-Disordered Rock-Salt Cathodes," *Journal of the American Chemical Society* 144 (2022): 19838–19848.

41. R. E. Ruther, A. F. Callender, H. Zhou, S. K. Martha, and J. Nanda, "Raman Microscopy of Lithium-Manganese-Rich Transition Metal Oxide Cathodes," *Journal of The Electrochemical Society* 162 (2014): A98–A102, https://doi.org/10.1149/2.0361501jes.

42. C. K. Chua, A. Ambrosi, and M. Pumera, "Graphene Oxide Reduction by Standard Industrial Reducing Agent: Thiourea Dioxide," *Journal of Materials Chemistry* 22 (2012): 11054–11061, https://doi.org/10.1039/c2jm16054d.

43. S. M. Tan, A. Ambrosi, C. K. Chua, and M. Pumera, "Electron Transfer Properties of Chemically Reduced Graphene Materials With Different Oxygen Contents," *Journal of Materials Chemistry A* 2 (2014): 10668–10675, https://doi.org/10.1039/C4TA01034E.

44. J. Ahn, R. Giovine, V. C. Wu, et al., "Ultrahigh-Capacity Rocksalt Cathodes Enabled by Cycling-Activated Structural Changes," *Advanced Energy Materials* 13 (2023): 2300221, https://doi.org/10.1002/aenm.202300221.

45. T. Holstun, T. P. Mishra, L. Huang, et al., "Accelerating the Electrochemical Formation of the δ Phase in Manganese-Rich Rocksalt Cathodes," *Advanced Materials* 37 (2024): 2412871, https://doi.org/10.1002/adma.202412871.

46. Z. Cai, B. Ouyang, H. M. Hau, et al., "In Situ Formed Partially Disordered Phases as Earth-Abundant Mn-Rich Cathode Materials," *Nature Energy* 9 (2024): 27–36, https://doi.org/10.1038/s41560-023-01375-9.

47. H. M. Hau, T. Holstun, E. Lee, et al., "Disordered Rocksalts as High-Energy and Earth-Abundant Li-Ion Cathodes," *Advanced Materials* 37 (2025): 2502766, https://doi.org/10.1002/adma.202502766.

48. H. Lohani, V. S. Avvaru, S. Jeong, and H. Kim, "Developing Low-Cost Rechargeable Batteries: Beyond Traditional Layered Oxide Cathodes for Li-Ion and Beyond Li-Ion Batteries," *Chemical Communications* 62 (2026): 793–813, https://doi.org/10.1039/D5CC05642J.

49. J. Huang, P. Zhong, Y. Ha, et al., "Non-Topotactic Reactions Enable High Rate Capability in Li-Rich Cathode Materials," *Nature Energy* 6 (2021): 706–714, https://doi.org/10.1038/s41560-021-00817-6.

50. S. Sharifi-Asl, F. A. Soto, T. Foroozan, et al., "Anti-Oxygen Leaking $LiCoO_2$," *Advanced Functional Materials* 29 (2019): 1901110, https://doi.org/10.1002/adfm.201901110.

51. F. Ning, H. Shang, B. Li, N. Jiang, R. Zou, and D. Xia, "Surface Thermodynamic Stability of Li-Rich Li_2MnO_3: Effect of Defective Graphene," *Energy Storage Materials* 22 (2019): 113–119, https://doi.org/10.1016/j.ensm.2019.01.004.

52. K. Zhou, C. Zhang, Y. Li, et al., "A Critical Evaluation of Interfacial Stability in Li-Excess Cation-Disordered Rock-Salt Oxide Cathode," *Chemical Engineering Journal* 464 (2023): 142709, https://doi.org/10.1016/j.cej.2023.142709.

53. T. Y. Huang, Z. Cai, M. J. Crafton, et al., "Chemical Origin of in Situ Carbon Dioxide Outgassing From a Cation-Disordered Rock Salt Cathode," *Chemistry of Materials* 36 (2024): 6535–6546, https://doi.org/10.1021/acs.chemmater.4c00756.

54. B. Zhou, S. An, D. Kitsche, et al., "Improved Performance of High-Entropy Disordered Rocksalt Oxyfluoride Cathode by Atomic Layer Deposition Coating for Li-Ion Batteries," *Small Structures* 5 (2024): 2400005, https://doi.org/10.1002/sstr.202400005.

55. H. Zhang, H. Liu, L. F. J. Piper, M. S. Whittingham, and G. Zhou, "Oxygen Loss in Layered Oxide Cathodes for Li-Ion Batteries: Mechanisms, Effects, and Mitigation," *Chemical Reviews* 122 (2022): 5641–5681, https://doi.org/10.1021/acs.chemrev.1c00327.

56. T. Li, X. Xia, J. Liu, et al., "Suppressing Surface Lattice Oxygen Evolution by Fluorinated Graphene-Scaffolded Lithium-Rich Manganese-Based Cathode for Enhanced Stability," *Energy Storage Materials* 49 (2022): 555–563, https://doi.org/10.1016/j.ensm.2022.05.002.

57. D. Huang, C. Engtrakul, S. Nanayakkara, et al., "Understanding Degradation at the Lithium-Ion Battery Cathode/Electrolyte Interface: Connecting Transition-Metal Dissolution Mechanisms to Electrolyte Composition," *ACS Applied Materials & Interfaces* 13 (2021): 11930–11939, https://doi.org/10.1021/acsami.0c22235.

58. M. J. Crafton, Y. Yue, T. Y. Huang, W. Tong, and B. D. McCloskey, "Anion Reactivity in Cation-Disordered Rocksalt Cathode Materials: The Influence of Fluorine Substitution," *Advanced Energy Materials* 10 (2020): 2001500, https://doi.org/10.1002/aenm.202001500.

59. L. Rynearson, C. Antolini, C. Jayawardana, M. Yeddala, D. Hayes, and B. L. Lucht, "Speciation of Transition Metal Dissolution in Electrolyte from Common Cathode Materials," *Angewandte Chemie International Edition* 63 (2024): 202317109.

60. J. P. Allen, C. A. O'Keefe, and C. P. Grey, "Quantifying Dissolved Transition Metals in Battery Electrolyte Solutions With NMR Paramagnetic Relaxation Enhancement," *The Journal of Physical Chemistry C* 127 (2023): 9509–9521, https://doi.org/10.1021/acs.jpcc.3c01396.

61. E. Lee, D. H. Lee, S. Bessette, et al., "Nearly All-Active-Material Cathodes Free of Nickel and Cobalt for Li-Ion Batteries," *Energy & Environmental Science* 17 (2024): 3753–3764, https://doi.org/10.1039/D4EE00551A.

62. M. S. Chambers, T. Li, Z. Liang, et al., "Exploring a New Synthesis Route to Lithium-Excess Disordered Rock Salt (DRX) Cathode Materials," *Materials Advances* 6 (2025): 2990–3001.

63. H. Cha, J. Kim, H. Lee, et al., "Boosting Reaction Homogeneity in High-Energy Lithium-Ion Battery Cathode Materials," *Advanced Materials* 32 (2020): 2003040, https://doi.org/10.1002/adma.202003040.

64. A. Shrivastava, N. Sharma, X. He, Y. Liu, and K. Zhao, "On the Scale of Heterogeneity in Composite Electrodes of Batteries," *Proceedings of the National Academy of Sciences* 122 (2025): 2520136122, https://doi.org/10.1073/pnas.2520136122.

65. Z. Ruff, C. Xu, and C. P. Grey, "Transition Metal Dissolution and Degradation in NMC811-Graphite Electrochemical Cells," *Journal of The Electrochemical Society* 168 (2021): 060518, https://doi.org/10.1149/1945-7111/ac0359.

66. B. D. McCloskey, R. Scheffler, A. Speidel, D. S. Bethune, R. M. Shelby, and A. C. Luntz, "On the Efficacy of Electrocatalysis in Nonaqueous Li–O_2 Batteries," *Journal of the American Chemical Society* 133 (2011): 18038–18041, https://doi.org/10.1021/ja207229n.

Supporting Information

Additional supporting information can be found online in the Supporting Information section.

Supporting File: adfm76964-sup-0001-SuppMat.docx.